

# The $^{12}\text{CO}/^{13}\text{CO}$ ratio in turbulent molecular clouds

László Szűcs<sup>\*†</sup>, Simon C. O. Glover & Ralf S. Klessen

*Universität Heidelberg, Zentrum für Astronomie, Institut für Theoretische Astrophysik  
Albert-Ueberle-Str. 2, D-69120 Heidelberg, Germany*

14 December 2018

## ABSTRACT

Carbon monoxide (CO) isotopes are commonly used as tracers of column density in studies of the interstellar medium. The most abundant CO isotope,  $^{12}\text{CO}$ , is usually optically thick in intermediate and high density regions and so provides only a lower limit for the column density. In these regions, less abundant isotopes, such as  $^{13}\text{CO}$  are observed. When these  $^{13}\text{CO}$  observations are then used to infer  $^{12}\text{CO}$  column densities, a uniform  $^{12}\text{CO}/^{13}\text{CO}$  isotope ratio is often adopted. A similar approximation is also frequently made when comparing results from cloud simulations including chemistry to observations of real clouds.

In this work, we examine the impact of two effects – the selective photodissociation and chemical fractionation of CO – on the  $^{12}\text{CO}/^{13}\text{CO}$  isotopic ratio, with the aim of testing the validity of a uniform scaling between  $^{12}\text{CO}$  and  $^{13}\text{CO}$ . We follow the coupled chemical, thermal and dynamical evolution of isolated, starless molecular clouds with several different metallicities, radiation fields and initial densities, and then post-process them with line radiative transfer in order to obtain maps of the emergent  $^{13}\text{CO}$  emission.

We find that the CO isotope ratio shows a close correlation to both the  $^{12}\text{CO}$  and the  $^{13}\text{CO}$  column densities, with only a weak dependence on the cloud properties. The ratio varies within a factor of 2–3 with the CO isotope column density. When a uniform ratio is assumed, this results in up to 60 per cent error in  $^{12}\text{CO}$  column density and mass estimates derived from observed  $^{13}\text{CO}$  column density. The same assumption results in up to 50 per cent difference in the intensity of  $^{13}\text{CO}$  emission maps derived from  $^{12}\text{CO}$  number density distributions. We show that this effect can be corrected by the use of a fitting formula derived from our simulations. The formula describes the correlation between the isotope ratio and the  $^{12}\text{CO}$  or the  $^{13}\text{CO}$  column density. The proposed formula is consistent with millimetre-wavelength measurements of the CO isotope ratio, but underestimates the ratios from ultraviolet (UV) absorption data. We discuss the possible reasons for the discrepancy. The fitting formula nevertheless allows us to obtain more accurate  $^{13}\text{CO}$  emission maps from simulations and to estimate the isotope ratio – therefore the  $^{12}\text{CO}$  column density – from  $^{13}\text{CO}$  observations.

**Key words:** astrochemistry – hydrodynamics – radiative transfer – ISM: abundances – radio lines: ISM

## 1 INTRODUCTION

The carbon monoxide molecule (CO) and its isotopes are the most widely used gas-phase tracers of total column density in the interstellar medium (ISM). In contrast to the hydrogen molecule, CO is asymmetric and hence has a permanent dipole moment. Its dipole transitions between rotational levels can be excited at temperatures (few  $\times 10$  K)

and densities ( $\approx 300 \text{ cm}^{-3}$ ) typical of giant molecular clouds (GMCs). The emission from the lowest transitions is relatively easily detectable at millimetre wavelengths. Due to its high fractional abundance ( $\chi_{\text{CO}} \approx 10^{-4}$ , in equilibrium at high density) the emission of the most abundant CO isotope ( $^{12}\text{CO}$ ) is usually optically thick, therefore only lower limits of the total column density could be derived. To achieve better total column density estimates, less abundant CO isotopes are used (usually  $^{13}\text{CO}$  and  $\text{C}^{18}\text{O}$ ). The simplest and most often used method is the following (e.g. [Pineda et al. 2008](#); [Wilson 2009](#); [Pineda et al. 2010](#)): The  $^{12}\text{CO}$  emission is assumed to be fully optically thick and in local thermody-

<sup>\*</sup> Member of IMPRS for Astronomy & Cosmic Physics at the University of Heidelberg.

<sup>†</sup> szucs@uni-heidelberg.de

namic equilibrium (LTE), allowing the excitation temperature of  $^{12}\text{CO}$  to be calculated. If the excitation temperature is the same for  $^{13}\text{CO}$  and if  $^{13}\text{CO}$  is optically thin, a simple relation between the integrated intensity along the line of sight,  $W(^{13}\text{CO})$ , and the column density of  $^{13}\text{CO}$ ,  $N(^{13}\text{CO})$  can be derived (e.g. see equation 9 in [Pineda et al. 2008](#)). The  $^{13}\text{CO}$  column densities are then usually converted into  $^{12}\text{CO}$  column densities using a globally constant (i.e. uniform)  $^{12}\text{CO}/^{13}\text{CO}$  isotope ratio. Finally, the  $^{12}\text{CO}$  column density is transformed to total column density assuming a given conversion factor between CO and  $\text{H}_2$ . The high uncertainties and environmental dependence of this final step have been studied in the literature ([Shetty et al. 2011a,b](#); [Glover & Mac Low 2011](#); [Feldmann et al. 2012](#), and references within).

However, the  $^{12}\text{CO}/^{13}\text{CO}$  ratio may vary considerably. Typically it is chosen to be equal to the measured  $^{12}\text{C}/^{13}\text{C}$  ratio ([Pineda et al. 2010](#)). The carbon isotope ratio, however, shows large regional variations. Based on observations of millimetre-wavelength emission of CO isotopes, [Langer & Penzias \(1990\)](#) found a systematic gradient with galactocentric distance in the carbon isotope ratio, ranging from 24 in the Galactic Center to about 70 at  $\sim 12$  kpc. They found the average ratio to be 57 at the solar galactocentric distance, which shows  $^{13}\text{C}$  enhancement compared to the value of 89 measured in the Solar System ([Geiss 1988](#)). Observations of CO absorption in ultraviolet electronic and near-infrared vibrational transitions (e.g. [Scoville et al. 1983](#); [Mitchell & Maillard 1993](#); [Goto et al. 2003](#); [Sonnentrucker et al. 2007](#); [Sheffer et al. 2007](#)) find up to a factor of 3 higher ratios in the solar neighbourhood. Nevertheless, the most frequently adopted ratios are between 57 ([Langer & Penzias 1990](#)) and 69 ([Wilson 1999](#)), the measured average values for the local ISM.

The gradient with galactocentric distance and the  $^{13}\text{C}$  enhancement of the local ISM compared to the Solar System value could be interpreted in the framework of the carbon isotopic nucleosynthesis.  $^{12}\text{C}$  is the primary product of the triple-alpha process during the post Red Giant Branch (RGB) evolution of massive stars. The rarer  $^{13}\text{C}$  is produced from  $^{12}\text{C}$  as a secondary product in the CNO cycle during the RGB phase of low and intermediate mass stars. Due to the longer lifetime of low and intermediate mass stars – which are the main contributors of  $^{13}\text{C}$  enrichment – the  $^{12}\text{C}/^{13}\text{C}$  ratio is expected to decrease with time and to depend on the star formation history ([Audouze et al. 1975](#)).

More important for our problem, however, is the fact that the CO isotope ratio could vary by a factor of a few even if the initial  $^{12}\text{C}/^{13}\text{C}$  ratio is constant in a region under investigation, due to isotope-selective chemical processes. For example, [van Dishoeck & Black \(1988\)](#) describe qualitatively the CO isotopic chemistry in molecular clouds as follows (see Fig. 1). The preferred pathways of CO production are the ion-neutral reaction of  $\text{C}^+$  and OH producing  $\text{HCO}^+$ , which dissociatively recombines to CO and H, and the neutral-neutral reaction of CH or  $\text{CH}_2$  with an oxygen atom. These reactions are not isotope-selective and work (with varying efficiency) in every region of the molecular

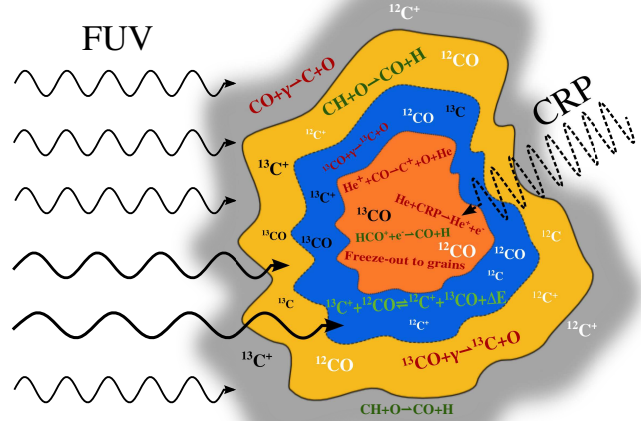
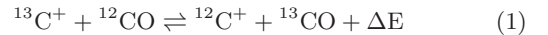


**Figure 1.** Qualitative picture of carbon isotopic chemistry in molecular clouds. The outer diffuse layer (gray) is followed by the translucent (yellow and blue) and the inner, dense regions (orange). The font size of the chemical species relates to the abundance of the species in the region. The font size of chemical reactions indicates the importance of the reaction in the region, the green and red colors represent reactions producing and destroying CO. When a particular isotopic species is not indicated, then both species are affected. Based on [van Dishoeck & Black \(1988\)](#).

cloud. In the diffuse regions (gray,  $A_V < 0.5 \text{ mag}^1$ ) the photodissociation of CO by interstellar far-ultraviolet (FUV) photons dominates over the production reactions and most of the carbon is in ionized form. In translucent regions (yellow,  $1 \text{ mag} < A_V < 2 \text{ mag}$ ) the CO production rates start to compete with the photodissociation. The  $^{12}\text{CO}$  column density becomes high enough to shield the  $^{12}\text{CO}$  from FUV photons. However,  $^{13}\text{CO}$ , due its lower number density and the slightly shifted absorption lines, is less effectively shielded. This selective photodissociation leads to an increased isotope ratio. Further in (blue,  $2 \text{ mag} < A_V < 5 \text{ mag}$ ), due to the shielding by dust absorption and the increasing  $^{13}\text{CO}$  column density both isotopic species are effectively protected from FUV photons. In this region ionized carbon is still abundant and the



fractionation reaction ([Watson et al. 1976](#)) becomes important. At temperatures typical to the corresponding cloud depths, the exothermic reaction (to the right, leads to energy release) is preferred, resulting in more  $^{13}\text{CO}$  production, and consequently in a reduced isotope ratio. At the highest column densities (orange,  $A_V > 5 \text{ mag}$ ) the production and destruction of CO isotopes are dominated by the non-isotope-selective  $\text{HCO}^+$  recombination and dissociative charge transfer with  $\text{He}^+$ . As a result, the isotope ratio approaches to the elemental ( $^{12}\text{C}/^{13}\text{C}$ ) ratio. Due to these processes we expect that the CO isotope ratio varies significantly even within the same GMC. In fact, observational studies report a factor of a few region-by-region varia-

<sup>1</sup> The exact visual extinction values depend on the strength of the intermittent radiation field and the density distribution.

tion. In the case of the Taurus molecular cloud, the indirect measurements of Goldsmith et al. (2008) and Pineda et al. (2010) find isotope ratios between 30 and the canonical value of 69, suggesting  $^{13}\text{CO}$  enrichment.

The direct determination of the  $^{12}\text{CO}/^{13}\text{CO}$  ratio is usually difficult and restricted to a certain column density range. For instance, the ultraviolet and millimetre-wavelength absorption measurements, such as presented by Sheffer et al. (2007), Sonnentrucker et al. (2007) and Liszt & Lucas (1998), require suitable galactic or extragalactic background sources and CO column densities, which fall to the optically thin, diffuse regime ( $N(^{12}\text{CO}) < \text{few} \times 10^{16} \text{ cm}^{-2}$ ). Observations of millimetre-wavelength emission from GMCs (e.g. Pineda et al. 2008; Goldsmith et al. 2008; Pineda et al. 2010), however, usually trace the higher CO column density regions, where the isotope ratio-column density correlation is not constrained by observations, and therefore as a “best guess” a uniform isotope ratio is adopted.

The inverse problem emerges when  $^{13}\text{CO}$  emission is inferred from (magneto-)hydrodynamical simulations. The computational cost of the chemical modelling scales with the cube of the number of species considered (Glover & Clark 2012b). Even when only 14 self-consistently calculated (i.e. not described by conservation laws), non-equilibrium species are included in the network, the chemistry will often be the dominating factor in terms of computational cost, taking up to 90 per cent of the total computational time (Glover et al. 2010; Glover & Clark 2012b). For the practical reason of cost efficiency usually only the most common isotope,  $^{12}\text{CO}$  is included in the chemical networks. When observable quantities, like emission from rarer CO isotopes are inferred from such simulations (e.g. Beaumont et al. 2013) the canonical isotope ratio is adopted and assumed to be constant through the whole simulation domain.

In this paper we investigate the effect of *selective photodissociation and chemical fractionation* on the  $^{12}\text{CO}/^{13}\text{CO}$  isotopic ratio in different environments and for different cloud properties, using turbulent hydrodynamical simulations that include a self-consistent chemical and cooling model and an approximate treatment of the attenuation of the interstellar radiation field (ISRF). One of our aims is to test and improve the frequently used assumption of uniform  $^{12}\text{CO}/^{13}\text{CO}$  ratio in the context of inferring  $^{13}\text{CO}$  emission from simulations which neglect isotopic chemistry. We also provide a prescription for deriving the isotope ratio from the  $^{13}\text{CO}$  column density (e.g. calculated from observations).

In section 2 we describe the numerical setup and the initial conditions of our simulations. Section 3 discusses the correlation between various (total,  $^{12}\text{CO}$  and  $^{13}\text{CO}$ ) column densities and the isotope ratio for different cloud conditions. We also propose a formula for inferring  $^{13}\text{CO}$  column/number densities from  $^{12}\text{CO}$  in simulations neglecting fractionation chemistry, and one for calculating the isotope ratio from observations of  $^{13}\text{CO}$ . Then in section 4, we post-process the simulations with line radiative transfer to quantitatively compare the emergent  $^{13}\text{CO}$  emission maps in case of self-consistently calculated, column density dependently inferred and uniform isotope ratios. Section 5 compares our results to previous theoretical works and to observations of the  $^{12}\text{CO}/^{13}\text{CO}$  column density ratio. We summarize the results and draw our final conclusions in section 6.

**Table 1.** Model parameters and used snapshots

Model	$n_0$ [ $\text{cm}^{-3}$ ]	Metallicity [ $Z_\odot$ ]	ISRF [ $G_0$ ]	Time [Myr]
a	300	0.3	1	2.046
b	300	0.6	1	1.930
c	300	1	0.1	2.124
d	300	1	1	2.150
e	300	1	10	2.022
f	1000	1	1	0.973

Summary of model parameters. Each model cloud had  $10^4 M_\odot$  and an SPH mass resolution of  $0.5 M_\odot$ . In each case the analysed snapshots were chosen to be the last before sink particle formation.  $Z_\odot$  and  $G_0$  refer to the Solar metallicity and Draine radiation field strength (1.7 in units of the Habing (1968) field) respectively.

## 2 SIMULATIONS

We use a modified version of the smoothed particle hydrodynamics (SPH) code GADGET-2<sup>2</sup>, described by Springel (2005). The modifications include a sink particle algorithm (Bate et al. 1995; Jappsen et al. 2005; Federrath et al. 2010; Glover & Clark 2012a), a simplified model of the gas chemistry with radiative heating and cooling (Glover & Clark 2012b) and an approximate treatment of the attenuation of the ISRF (Clark et al. 2012). Stellar feedback from the formed sink particles is not included, an effect which could influence the CO isotope ratio in high density regions significantly. Therefore, we restrict our analysis and discussion to cloud properties before sink particle formation (i.e. to molecular clouds in an early stage of evolution).

### 2.1 Chemistry

We adopt the chemical network of Nelson & Langer (1999) (hereafter NL99) supplemented with the hydrogen chemistry of Glover & Mac Low (2007). The network was designed to follow CO formation and destruction over a wide density range in molecular clouds. It takes multiple CO formation pathways into account: a formation channel involving the composite  $\text{CH}_x$  (CH and  $\text{CH}_2$ ) species, another involving the composite  $\text{OH}_x$  (OH,  $\text{H}_2\text{O}$  and  $\text{O}_2$ ) species and a third route via the dissociative recombination of  $\text{HCO}^+$ . The destruction of CO could happen due to photodissociation, dissociative charge transfer with  $\text{He}^+$  or through proton transfer from  $\text{H}_3^+$  resulting in the conversion of CO to  $\text{HCO}^+$ . See Table 1 in Glover & Clark (2012b) for the full list of reactions and the Appendix B of Glover et al. (2010) for the adopted reaction rate coefficients.

Initially the NL99 network does not account for the  $^{13}\text{C}$ ,  $^{13}\text{C}^+$ ,  $^{13}\text{CO}$  and  $\text{H}^{13}\text{CO}^+$  isotopes. Therefore we add these species and the corresponding reactions, which are non-isotope-selective, from the original network. We do not apply rescaling on the reaction rate coefficients of these reactions. In addition, to allow conversion of  $^{12}\text{CO}$  to  $^{13}\text{CO}$ , we implemented the  $^{13}\text{CO}$  fractionation reaction (equation 1, with the left to right rate coefficient of  $R_{\text{frac},\text{CO},\text{lr}} = 2 \times 10^{-10} \text{ cm}^3 \text{ s}^{-1}$  and the temperature dependent right to left rate coefficient of  $R_{\text{frac},\text{CO},\text{rl}} = 2 \times 10^{-10} \exp(-35 \text{ K}/T_{\text{gas}}) \text{ cm}^3 \text{ s}^{-1}$ . Although, Smith & Adams

<sup>2</sup> <http://www.mpa-garching.mpg.de/gadget/>

(1980) suggests an order of magnitude higher rate coefficient, Sheffer et al. (2007) finds that the smaller value of Watson et al. (1976) is more consistent with the observations, therefore we adopt the latter. The  $^{12}\text{CO}$  and  $^{13}\text{CO}$  photodissociation rate coefficients for optically thin gas are taken to be equal with the value of  $R_{\text{pd,CO,thin}} = 1.235 \times 10^{-10} \text{ s}^{-1}$  (van Dishoeck & Black 1988).

## 2.2 Attenuation of the ISRF

As we describe in the introduction, the differential shielding of  $^{12}\text{CO}$  and  $^{13}\text{CO}$  plays an important role in determining the isotope ratio. To account for this effect the column densities – from the centre of a given SPH particle to the outer surface of the cloud – of the critical species ( $\text{H}_2$ , dust,  $^{12}\text{CO}$  and  $^{13}\text{CO}$ ) need to be calculated. We use the TreeCol method presented by Clark et al. (2012). In short, TreeCol is a cost efficient algorithm to calculate total and species specific column densities while “walking” the gravitational tree structure (used in GADGET-2 to compute the gravitational interaction of far-away particles). It constructs a HEALPIX (Górski et al. 2005) sphere with 48 equal-area pixels for each SPH particle and accumulates the contribution of the line of sight nodes for the considered pixel. We trace the total (proton),  $\text{H}_2$ ,  $^{12}\text{CO}$  and  $^{13}\text{CO}$  column densities. The visual extinction ( $A_V$ ) due to the dust is calculated using the formula (Bohlin et al. 1978; Draine & Bertoldi 1996),

$$A_V = \frac{N_{\text{tot}}}{1.8699 \times 10^{21} \text{ cm}^2} \times f_{\text{dg}}, \quad (2)$$

where  $N_{\text{tot}}$  is the total proton column density (hydrogen +  $4 \times$  helium nuclei) and  $f_{\text{dg}} = Z/Z_{\odot}$  is the factor correcting for the simulation metallicity.

We model the attenuation of the ISRF by multiplying the optically thin photodissociation rates with shielding factors depending on the column density and visual extinction. The  $\text{H}_2$  photodissociation rate is attenuated due to dust absorption and  $\text{H}_2$  self-shielding. The dust shielding factor can be calculated in the plane-parallel approximation by

$$\Theta_{\text{dust}} = \exp(-\gamma A_V) \quad (3)$$

with  $\gamma = 3.74$  (Draine & Bertoldi 1996). The self-shielding factor depends on the  $\text{H}_2$  column density and is calculated according to equation (37) in Draine & Bertoldi (1996). In the case of  $^{12}\text{CO}$  and  $^{13}\text{CO}$ , the shielding is due to dust absorption, the  $\text{H}_2$  Lyman-Werner lines and CO self-shielding. The shielding factor due to dust absorption for both isotopic species is given by equation (3) with  $\gamma = 2.5$ . We adopted the tabulated shielding factors from Lee et al. (1996) for CO shielding by  $\text{H}_2$  and self-shielding. We used the same relation between the column density and the CO self-shielding factor for both CO isotopes when calculating the self-shielding, but with the corresponding isotope column densities. Recently, Visser et al. (2009) provided updated CO self-shielding factors based on new spectroscopic data, however, the difference in the considered parameter range is thought to be marginal (Röllig & Ossenkopf 2013).

We refer to section 2.2 in Glover et al. (2010) for a more detailed description of the adopted treatment of photochemistry.

## 2.3 Thermal model

The temperature structure of the cloud has a large impact on the chemical fractionation (due to the temperature barrier for the right-to-left path) and a moderate effect on the selective photodissociation (more strongly isotope selective in colder gas). The latter effect is discussed in detail in Visser et al. (2009), but not considered here.

The adopted thermal model – with the complete list of heating and cooling processes – is discussed in section 3.2.4 and Fig. 8 in Glover & Clark (2012a). The dominant heating processes in our simulations are the photoelectric-, shock-, cosmic ray, and pdV heating. The major coolants at low and intermediate densities are  $\text{C}^+$  and CO, while at high density cooling is dominated by the dust. We consider the  $\text{C}^+$  and CO isotopes separately when calculating the cooling rates. The relative importance of radiative cooling via carbon isotopic species will be discussed in a follow-up paper.

## 2.4 Initial conditions

Our basic initial setup is identical to Glover & Clark (2012a). We start the simulations with a uniform density sphere with  $10^4 M_{\odot}$  total mass. The initial volume density of the sphere is set to 300 or 1000  $\text{cm}^{-3}$ , resulting in an approximate cloud radius of 6 pc or 4 pc, respectively. We give turbulent bulk motions to the cloud with the power spectrum of  $P(k) \propto k^{-4}$ , and total kinetic energy equal to the gravitational potential energy of the cloud. The non-thermal, turbulent motion is allowed to decay freely. The initial temperature is uniform at 20 K.

In case of the solar metallicity ( $Z_{\odot}$ ) runs, the adopted initial abundances of  $^{12}\text{C}$ ,  $^{13}\text{C}$  and O relative to hydrogen nuclei are  $x_{12\text{C}} = 1.4 \times 10^{-4}$ ,  $x_{13\text{C}} = 2.3 \times 10^{-6}$  and  $x_{\text{O}} = 3.2 \times 10^{-4}$  respectively (Sembach et al. 2000). Initially all hydrogen is in molecular and all carbon is in ionized forms. The neutral helium fractional abundance is 0.1 in all simulations. The total abundance of low ionization potential metals (Na, Mg, etc.) is  $x_M = 1 \times 10^{-7}$ . These are initially assumed to be fully ionized. The electron abundance of the cloud is set to give an overall neutral medium. To investigate the metallicity dependence of our results, we also perform simulations with scaled initial abundances geared towards the SMC ( $0.3 \times Z_{\odot}$ ) and the LMC ( $0.6 \times Z_{\odot}$ ). In each run the carbon isotopic abundance ratio is 60, a value consistent with the frequently adopted local ISM measurements (Lucas & Liszt 1998). Besides the abundances we also scale the dust-to-gas ratio with a factor ( $f_{\text{dg}} = Z/Z_{\odot}$ ). In the solar metallicity case the dust-to-gas ratio is taken to be 0.01.

We assume that the cloud is illuminated by an isotropic, standard radiation field, described by Draine (1978) in the UV and by Black (1994) at longer wavelengths. The default field strength is  $G_0 = 1.7$  in units of the Habing (1968) field, corresponding to  $2.7 \times 10^{-3} \text{ erg cm}^{-2} \text{ s}^{-1}$  integrated flux in the 91.2–240 nm wavelength range. To test various galactic environments we scaled the radiation field strength between  $0.1 \times G_0$  and  $10 \times G_0$  with the fiducial value of  $1 \times G_0$ .

In the most shielded regions of GMCs the primary CO destruction pathway is through dissociative charge transfer with  $\text{He}^+$ . The  $\text{He}^+$  is produced by the interaction of He



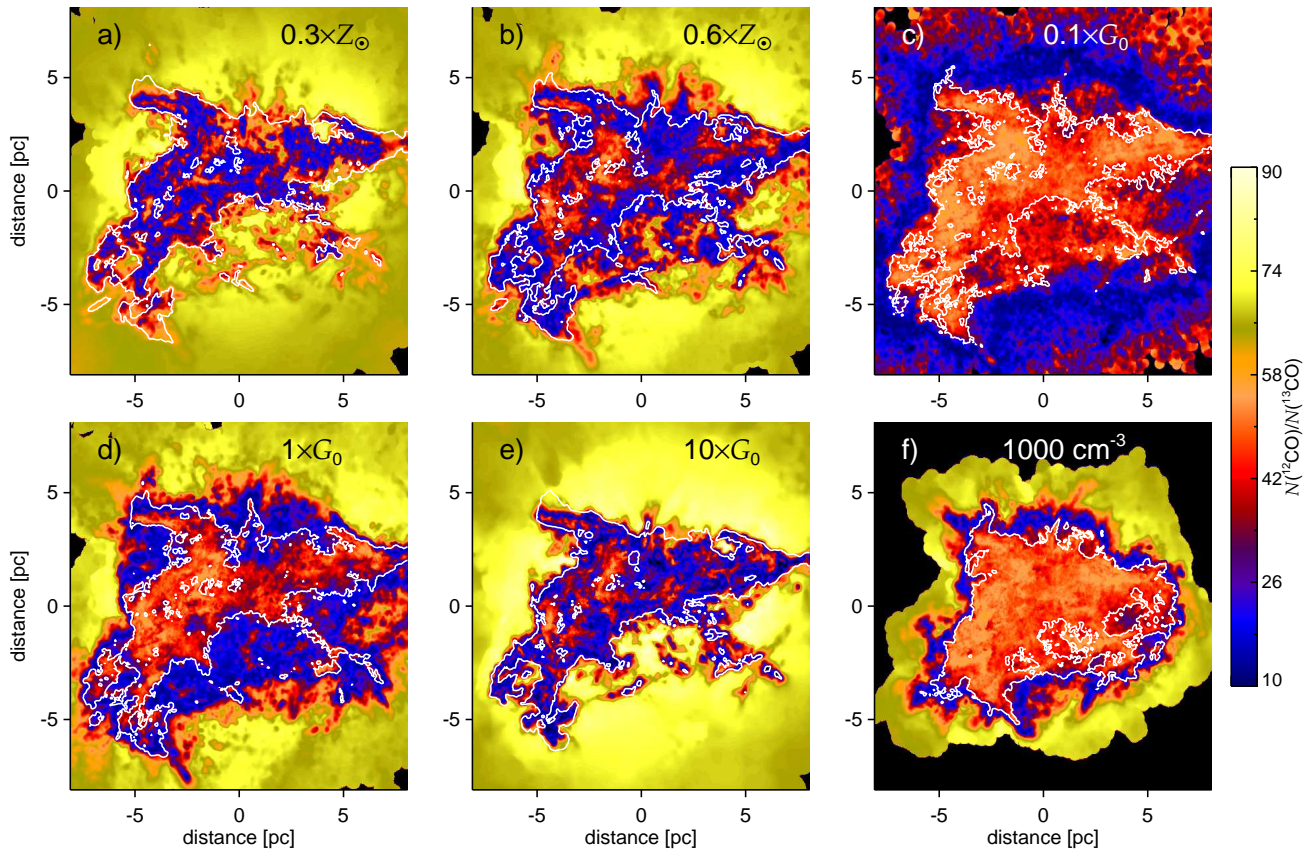


**Figure 2.**  $N(^{12}\text{CO})/N(^{13}\text{CO})$  column density ratio maps for varying ISRFs, metallicities and initial volume densities. The white contour represents the  $5 \times 10^{21} \text{ cm}^{-2}$  level in total column density. The same colour scale applies for all the ratio maps. Yellow, blue and orange colors mark regions dominated by selective photodissociation, fractionation and very high optical depth (lack of  $\text{C}^+$  ions) respectively. Lines of sight which do not intersect any SPH particles are marked with black.

with cosmic ray particles, which can penetrate deep into the cloud. The adopted cosmic ray ionization rate of atomic hydrogen is  $\zeta_{\text{H}} = 10^{-17} \text{ s}^{-1}$ . The ones for  $\text{H}_2$  and atomic He are  $2 \times \zeta_{\text{H}}$  and  $1.09 \times \zeta_{\text{H}}$ , respectively.

We performed 6 hydrodynamic cloud simulations in total. The parameters explored are summarized in Table 1. In the analysis that follows in section 3 we take simulation d) as the fiducial model.

### 3 THE $^{12}\text{CO}/^{13}\text{CO}$ COLUMN DENSITY RATIO

In this section we analyse the  $N(^{12}\text{CO})/N(^{13}\text{CO})$  isotopic column density ratio resulting from our simulations. We look for correlations between the isotope ratio and the total,  $^{12}\text{CO}$  and  $^{13}\text{CO}$  column densities. Hereafter, if not indicated otherwise, the column densities are meant as the number of atoms/molecules of a species or the gas mass in a given line of sight, per  $\text{cm}^2$ , integrated from the “observer” to infinity.

We used the grid interpolated quantities (see Appendix A). The column density maps were calculated by integrating the volume density along the  $z$  direction of the grid. Although the apparent shape of the molecular cloud does depend on the viewing direction, the quantities and relationships discussed below are independent of the choice of viewing direction. Fig. 2 shows the ratio of  $^{12}\text{CO}$  and  $^{13}\text{CO}$

column density maps for different radiation fields, metallicities and initial volume densities. The white contour line indicates the total column density level of  $5 \times 10^{21} \text{ cm}^{-2}$ . The shape of this contour line does not change substantially with varying radiation field strength or metallicity, indicating that the overall density structure is not affected significantly within the studied parameter range (see also Fig. 3).

The simulated ratio maps are in good agreement with the picture of the CO isotopic chemistry described in the introduction. In the outer parts of the clouds, the total column densities are low and shielding is ineffective. Despite this, some CO remains in these regions. In this gas, selective photodissociation of  $^{13}\text{CO}$  dominates, increasing the  $^{12}\text{CO}/^{13}\text{CO}$  ratio to  $\sim 75$  (yellow region). Further in, where the shielding of  $^{13}\text{CO}$  becomes more effective, the fractionation reaction takes over and significantly decreases the ratio to  $\sim 25$  (blue region). At the core of the cloud, the radiation field photodissociates CO or ionizes C with a very low rate, and so neither of the isotope-selective processes are effective. In these regions the  $N(^{12}\text{CO})/N(^{13}\text{CO})$  ratio increases again and approaches the initially set  $^{12}\text{C}/^{13}\text{C}$  ratio (marked by the orange color). Qualitatively all simulations follow this scheme. However, the quantitative details – e.g the transitional column densities – differ considerably from simulation to simulation.

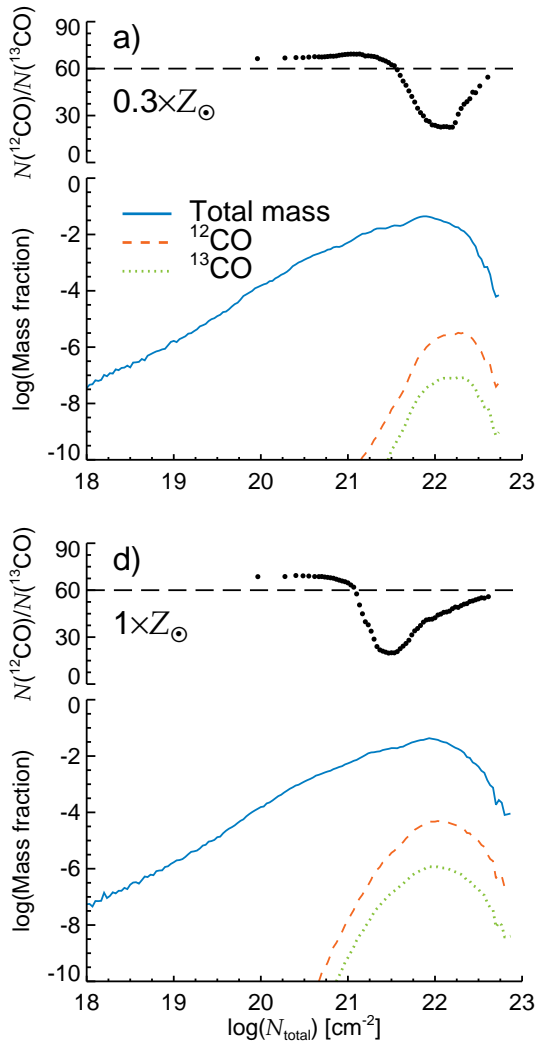


**Figure 3.** Total,  $^{12}\text{CO}$  and  $^{13}\text{CO}$  mass fraction distributions and the  $N(^{12}\text{CO})/N(^{13}\text{CO})$  ratio as a function of the total column density for low metallicity (a) and the fiducial (d) simulations. The total column density distributions are roughly identical, while CO forms at a factor of 5 higher column densities in the case of a). The total CO mass is also reduced by about an order of magnitude. The dip in the isotope ratio curve is shifted by almost a order of magnitude to higher total column densities. Note that the column density ratio is not expected to be equivalent to the ratio of the  $^{12}\text{CO}$  and  $^{13}\text{CO}$  mass distributions, as in the latter case the area associated with a column density value is also taken into account.

### 3.1 Correlation with the total column density

The mass-weighted probability density distributions of the total, the  $^{12}\text{CO}$  and the  $^{13}\text{CO}$  column densities for simulations a) and d) are presented in Fig. 3. The figure shows the mass fraction of the cloud at a given column density. The CO isotope column densities are weighted with the total mass, therefore the corresponding curves show the cloud mass fraction locked in CO isotopes as a function of the total column density.

The overall density distributions in these simulations are roughly identical. The CO isotope distributions, however, show large differences: due to less effective shielding,

in simulation a) both CO isotopes form at a factor of a few higher total column densities and the total  $^{12}\text{CO}$  mass (the integral of the red curve multiplied by the total cloud mass) is also a factor of 20 lower,  $0.43 M_{\odot}$  and  $8.1 M_{\odot}$  for simulation a) and d) respectively. The total  $^{13}\text{CO}$  mass is reduced by a similar factor. Consequently, depending on cloud properties and environment, CO isotopes trace different total column densities and cloud mass fractions. Also note the relatively large fraction of the so called CO-dark gas, i.e. mass not traced at all by CO.

The upper sub-panels in Fig. 3 show the mean  $N(^{12}\text{CO})/N(^{13}\text{CO})$  ratio as a function of the total column density. The description of the algorithm that we used to produce these curves is given in section 3.3. The gradients of the curves represent the transitions between regions dominated by selective photodissociation, chemical fractionation and strong attenuation. The total column densities corresponding to these transitions are strongly dependent on the strength of the ISRF and the metallicity of the cloud. In case of simulation d) the  $5 \times 10^{21} \text{ cm}^{-2}$  total column density contour (see Fig. 2) approximately indicates the transition between the regions dominated by fractionation and strong shielding. In the case of simulation a), the reduced metallicity decreases both the CO column densities and the extinction due to dust that a parcel of gas in the cloud “sees”, resulting in less effective attenuation of the radiation field. The transition between the chemical fractionation-dominated and the attenuation-dominated regions is shifted to a total column density that is an order of magnitude larger. In this case, the  $5 \times 10^{21} \text{ cm}^{-2}$  contour line traces the transition between the regions dominated by selective photodissociation and chemical fractionation. Simulations with reduced metallicity or increased ISRF (b and e) behave similarly to model a), while simulation f) has transitional column densities similar to model d). In case of c), due to the weak radiation field, the selective photodissociation is inefficient even at the lowest column densities. The chemical fractionation dominated region is extended and this simulation produces the lowest  $^{12}\text{CO}/^{13}\text{CO}$  ratios, around the value of 15.

Regardless of the model dependent transitional total column densities, the isotope ratio seems to be consistent within a few per cent in the corresponding regions of the cloud for each simulation. In the selective photodissociation dominated region the ratio is about 70. In the region of chemical fractionation, the ratio drops to  $\sim 20$ . Finally, in the most shielded regions the CO isotope ratio approaches the initially set  $^{12}\text{C}/^{13}\text{C}$  ratio. Note, however, that the results from the outermost regions of the cloud are – due to large smoothing lengths and low SPH resolution – somewhat uncertain. These regions are usually also undetectable in CO emission, because of their very low column densities.

Fig. 3 also shows that the region of  $^{13}\text{CO}$  enhancement coincides with the highest CO mass fraction in case of simulation a) and with lower mass fractions in case of d). This indicates a higher importance of isotope-selective reactions when the radiation field is high and/or the metallicity is low.

We conclude that the total column density and the isotope ratio correlate, but the correlation strongly depends on the cloud properties and environment.

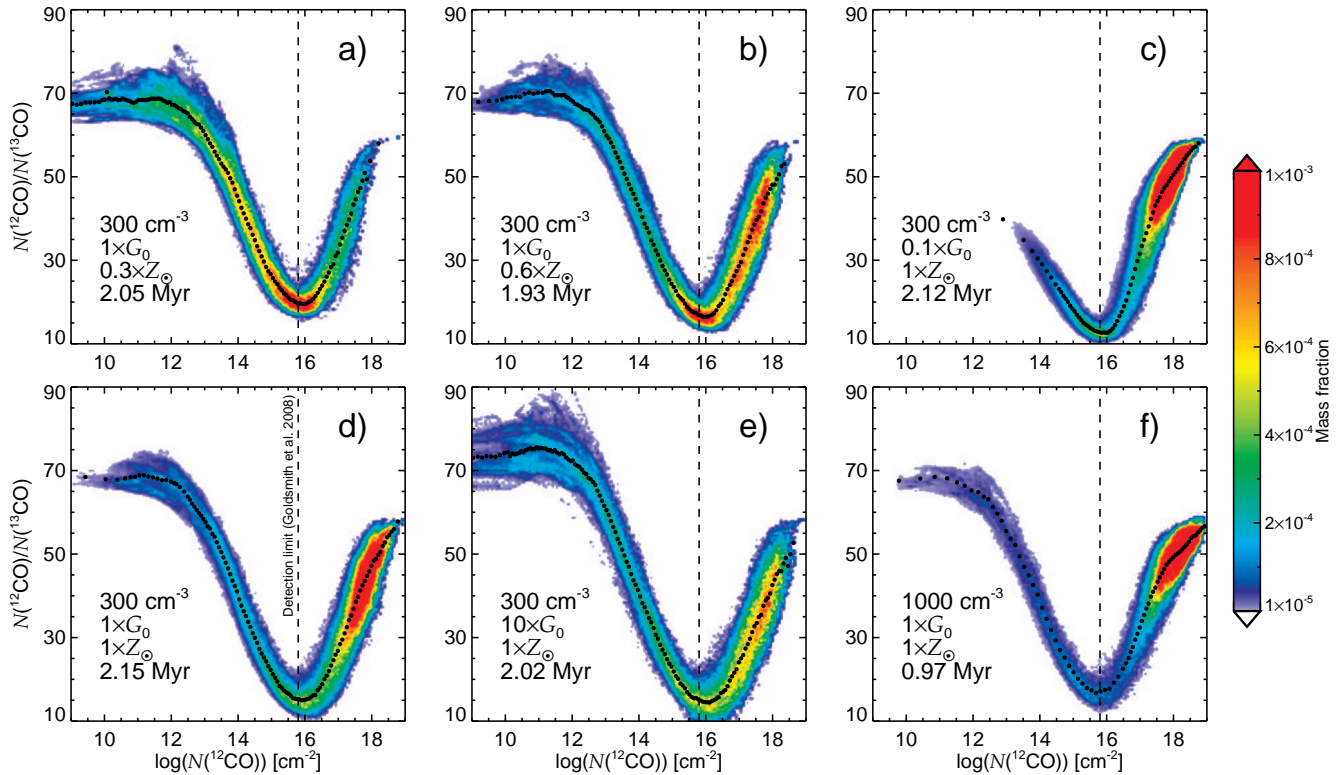


**Figure 4.** CO isotope column density ratio as a function of the  $^{12}\text{CO}$  column density, calculated using the “real” column densities (i.e. directly from the hydrodynamic simulation). Model parameters are indicated in the legend, the vertical line shows the approximate detection limit achieved by Goldsmith et al. (2008) in the case of the Taurus molecular cloud region. The colour indicates the mass fraction of the cloud with the specified  $^{12}\text{CO}$  column density and isotope ratio, which depends significantly on the model parameters. At low column densities, selective photodissociation increases the ratio up to 70. At higher column densities, the fractionation reaction takes over, resulting in a pronounced dip. The observations are sensitive to the inner regions of the cloud, where the fractionation reaction becomes less effective as the  $\text{C}^+$  abundance decreases, and the ratio increases to the initial value. The black dotted curves represents the fitted relation between the quantities (see Section 3.3).

### 3.2 Correlation with the $^{12}\text{CO}$ column density

We find a tighter correlation between the  $^{12}\text{CO}$  column density and the CO isotope ratio. Fig. 4 shows the mass-weighted, two dimensional probability density distribution of  $N(^{12}\text{CO})$  and the isotope ratio for the 6 simulations. The colours indicate the mass fraction of the cloud with a given parameter combination. Consistent with Fig. 3, most of the cloud mass lies at different  $^{12}\text{CO}$  column densities, depending on the model parameters. If the metallicity is low or the radiation field is strong, then CO forms at, and therefore traces, higher total column densities.

The most remarkable feature of Fig. 4 is that the location and depth of the dip in the isotope ratio shows only weak parameter dependence. The three dimensional nature ( $N(^{12}\text{CO})$  vs. isotope ratio vs. mass fraction) of these probability density distribution diagrams, however, makes it hard to directly compare them. Therefore, we project them into 2D space, keeping in mind that we are interested in the relationship of  $N(^{12}\text{CO})$  and the isotope ratio, and that we are aiming to derive a functional form. We construct curves according the following procedure: Starting from the low  $^{12}\text{CO}$  column densities we bin  $N(^{12}\text{CO})$  adaptively into strips. The normalized total mass fraction of a strip is required to be at least 0.002, a value chosen to provide well sampled isotope

ratio distribution in the strip. We then collapse the strip in the  $N(^{12}\text{CO})$  dimension by adding up mass fractions in isotope ratio bins. This gives the mass fraction in a  $N(^{12}\text{CO})$  strip as the function of isotope ratio. We fit a Gaussian to this curve to determine the mean value and the width of the distribution (i.e. the standard deviation). Finally, we determine an effective  $N(^{12}\text{CO})$  within the strip, by weighting based on the mass fraction contribution of a  $N(^{12}\text{CO})$  pixel column to the strip. We repeat this procedure until the upper limit of the  $^{12}\text{CO}$  column density is reached. The small, filled, black circles in the panels in Fig. 4 and the coloured filled symbols in Fig. 5 show the mean isotope ratios as a function of  $^{12}\text{CO}$  column density derived this way. Fig. 4 demonstrates that the derived mean ratios follow the probability density distribution well, justifying our approach.

The mean isotope ratio curves show a very good overall agreement in all cases (see Fig. 5). However, there is a weak correlation between the curve shape and the physical parameters. A higher initial density ( $n_0$ ) might result in higher isotope ratios at high  $^{12}\text{CO}$  column densities. As the metallicity increases from  $0.3 Z_\odot$  to  $1 Z_\odot$  the minimum isotope ratio seems to decrease from  $19.50 \pm 1.54$  to  $14.98 \pm 2.02$  (middle panel). The increasing radiation field strength seems to tilt the curve around  $N(^{12}\text{CO}) \approx 10^{16} \text{ cm}^{-2}$ , with increasing ratio below, and decreasing above the limit (right panel).



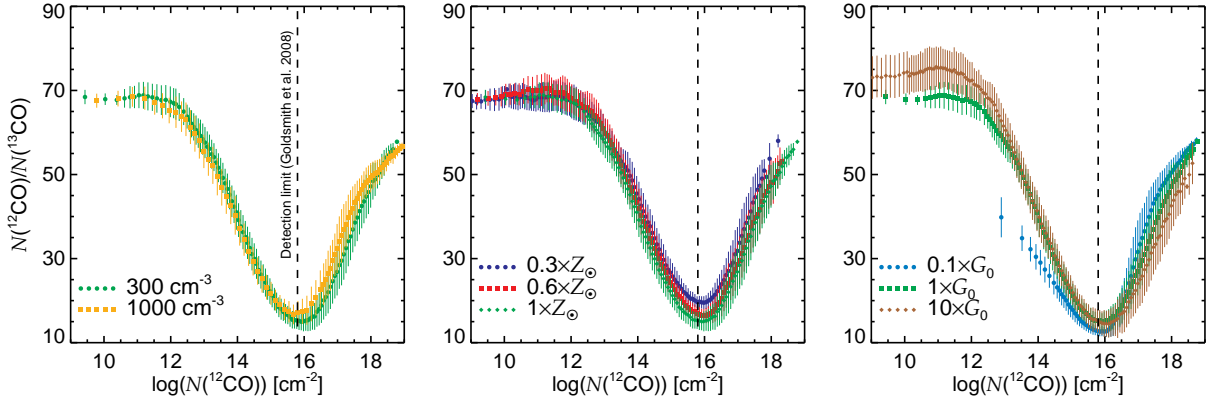


**Figure 5.** CO isotope column density ratio as a function of the  $^{12}\text{CO}$  column density derived by the procedure described in section 3.2. From left to right the panels compare the effect of varying the initial density, metallicity and radiation field. We emphasize that the main features of the curves only weakly depend on the physical parameters. We also note, however, that increasing the initial density seems to increase the isotope ratio at high densities, increasing the metallicity deepens the dip, while increasing the ISRF strength tends to increase the ratio at low  $N(^{12}\text{CO})$  and decrease it at high column densities. Model parameters not indicated in the legend are kept at the fiducial value.

The depth of the dip in the isotope ratio curve is expected to depend on the gas temperature (and therefore the heating and cooling processes) of the corresponding cloud regions. The chemical fractionation has an energy barrier for the right to left reaction path (see equation 1 and section 2.1), which is approximately 35 K. At temperature of a few hundred K the reaction could proceed in both directions with similar rate, resulting in a less enhanced  $^{13}\text{CO}$  abundance and a isotope ratio closer to the  $^{12}\text{C}/^{13}\text{C}$  ratio (e.g. Röllig & Ossenkopf 2013).

We emphasize, however, that these trends are not statistically significant in our simulations, and the model-by-model deviations of the isotope ratio curves are typically comparable to the standard deviations of the ratio. From this point on, we dispense with further investigation of the trends in the mean isotope ratio curves with physical parameters and assume that there is an unequivocal correlation between the  $^{12}\text{CO}$  column density and the  $^{12}\text{CO}/^{13}\text{CO}$  ratio and which is independent of the parameters we vary in the simulations.

### 3.3 Fitting formula

To derive a functional form for the  $N(^{12}\text{CO})$ -isotope ratio relationship we fit the curves presented in Fig. 5 individually and together using the non-linear least-squares Marquardt-Levenberg algorithm implemented in GNUPLT<sup>3</sup> (Williams et al. 2011). The combined data was constructed from all models except model c), due to its largely different behaviour at low  $^{12}\text{CO}$  column densities. We fitted 4th, 5th and 6th order polynomial functions taking the standard deviation of each data point into account. The best fit 4th order polynomial over-predicts the ratios for  $10^{15} \text{ cm}^{-2} < N(^{12}\text{CO}) < 10^{17} \text{ cm}^{-2}$ , and under-predicts in every other case. The 6th order polynomial does not provide a significantly better fit than the 5th order polynomial,

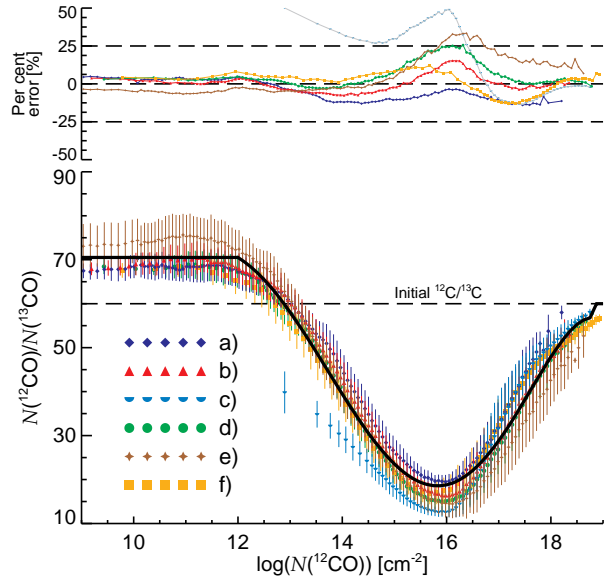


**Figure 6.** Similar to Fig. 5. Here we compare the  $N(^{12}\text{CO})$ -isotope ratio curves derived from the simulation (coloured dotted lines) to the adopted fitting formula (black solid line). The upper panel shows the percentage error of the formula when compared to the model data.

therefore we chose to use the best fitting 5th order polynomial for the further analysis. The best fitting polynomial coefficients are presented in Table 2 for the individual and the combined data.

We adopt the best fit coefficients for the combined model with the modifications that the ratio at  $^{12}\text{CO}$  column densities lower than  $10^{12} \text{ cm}^{-2}$  is equal to the ratio at  $N(^{12}\text{CO}) = 10^{12} \text{ cm}^{-2}$  and we set the ratio to 60 above an upper limit of  $N(^{12}\text{CO}) = 10^{19} \text{ cm}^{-2}$ . The final form of our

<sup>3</sup> <http://gnuplot.sourceforge.net/>



**Table 2.** Coefficients of the best fitting polynomials in case of the  $^{12}\text{CO}$  column density–isotope ratio correlation

Model	$a_{0,12}$	$a_{1,12}$	$a_{2,12}$	$a_{3,12}$	$a_{4,12}$	$a_{5,12}$
a	8830.28±837.30	-3417.74±327.70	519.44±50.64	-38.3318±3.862	1.36976±0.1454	-0.018945±0.00216
b	15143.40±739.80	-5864.96±282.60	893.56±42.64	-66.5346±3.176	2.41876±0.1168	-0.034358±0.00169
c	-11638.30±22850.00	1436.32±7212.00	122.18±907.40	-27.6231±56.88	1.50621±1.776	-0.0268676±0.02211
d	18808.00±499.10	-7225.33±184.60	1093.34±26.98	-81.0460±1.948	2.94005±0.0695	-0.0417669±0.00098
e	15887.60±450.70	-6190.23±169.90	949.30±25.29	-71.1792±1.860	2.60694±0.0676	-0.0373333±0.00097
f	21361.60±1320.00	-8193.56±474.90	1240.04±67.55	-92.1411±4.751	3.35797±0.1653	-0.0480218±0.00227
combined	16025.80±489.50	-6253.88±182.80	960.46±26.93	-72.1457±1.957	2.64822±0.0703	-0.038021±0.00099

**Table 3.** Coefficients of the best fitting polynomials in case of the  $^{13}\text{CO}$  column density–isotope ratio correlation

Model	$a_{0,13}$	$a_{1,13}$	$a_{2,13}$	$a_{3,13}$	$a_{4,13}$	$a_{5,13}$
a	-11985.70±6310.00	4672.87±2455.00	-727.18±379.70	57.075±29.190	-2.2690±1.1160	0.03657±0.01695
b	16827.90±2754.00	-6778.91±1056.00	1083.48±160.80	-85.274±12.170	3.2952±0.4576	-0.04995±0.00684
c	154967.00±19710.00	-57138.40±6958.00	8386.12±978.70	-611.968±68.550	22.1928±2.3910	-0.31983±0.03324
d	27661.40±2617.00	-10942.50±993.2	1720.04±149.80	-133.673±11.230	5.1250±0.4182	-0.07746±0.00619
e	3105.20±6375.00	-1384.49±2428.00	244.48±367.50	-20.709±27.630	0.83586±1.0320	-0.01284±0.01531
f	32829.10±3411.00	-13160.60±1283.00	2095.97±191.50	-165.140±14.200	6.42597±0.5226	-0.09871±0.00764
combined	58005.00±3172.00	-22880.10±1192.00	3585.13±178.00	-278.30±13.19	10.6906±0.4853	-0.16248±0.00710

fitting formula is

$$r(N_{12}) = \begin{cases} r(N_{12} = 10^{12}) & \text{if } N_{12} < 10^{12} \\ a_{0,12} + a_{1,12} \log_{10}(N_{12}) \\ + a_{2,12} \log_{10}(N_{12})^2 \\ + a_{3,12} \log_{10}(N_{12})^3 \\ + a_{4,12} \log_{10}(N_{12})^4 \\ + a_{5,12} \log_{10}(N_{12})^5 & \text{if } 10^{12} \leq N_{12} \leq 10^{19} \\ 60 & \text{if } 10^{19} < N_{12} \end{cases} \quad (4)$$

where  $r$  is the  $^{12}\text{CO}/^{13}\text{CO}$  ratio and  $N_{12}$  is the  $^{12}\text{CO}$  column density in units of  $\text{cm}^{-2}$ . To justify this choice we compare the function derived from the combined models to the individual models. The bottom panel of Fig. 6 shows the unmodified curves from section 3.2 for all models with the standard deviations represented by the vertical lines. The black line represent the fitting function. The top panel show the per cent error between the data points from the models and the approximate value from the formula,  $\Delta = (\text{function} - \text{data})/\text{data} \times 100$ . The deviation with which the formula reproduces the data tends to be the largest in the fractionation reaction dominated region ( $10^{15} \text{cm}^{-2} < N(^{12}\text{CO}) < 10^{16} \text{cm}^{-2}$ ) going up to about 30–35 per cent. Note however, the difference on the whole  $^{12}\text{CO}$  column density range ( $\leq 20$  per cent) is comparable to the standard deviation (i.e. the thickness) of the combined distribution.

### 3.4 Application for $^{13}\text{CO}$ observations

The  $^{12}\text{CO}/^{13}\text{CO}$  isotopic ratio shows a similar correlation with the  $^{13}\text{CO}$  column density as presented in section 3.2 and a fitting formula could also be derived following the procedure described in section 3.3. We adopt a similar functional form:  $r(N_{13}) = a_{0,13} + a_{1,13} \log_{10}(N_{13}) +$

$a_{2,13} \log_{10}(N_{13})^2 + a_{3,13} \log_{10}(N_{13})^3 + a_{4,13} \log_{10}(N_{13})^4 + a_{5,13} \log_{10}(N_{13})^5$ , where  $r$  and  $N_{13}$  are the isotope ratio and the  $^{13}\text{CO}$  column density, respectively. The best fitting coefficients for the individual runs and the combined sample are presented in Table 3. The fitting formula is valid for  $^{13}\text{CO}$  column densities in the range  $3 \times 10^{10} \text{cm}^3 - 5 \times 10^{16} \text{cm}^3$ . We do not consider lines of sight with column densities less than the lower value and set the isotope ratio to 60 in case of column densities higher than the upper limit. We exclude run c) from the combined sample.

Table 4 shows the total  $^{12}\text{CO}$  mass in the model, calculated with various methods. In case of the “real” mass, we use the self-consistently calculated  $^{12}\text{CO}$  distribution. In the uniform ratio case we take the  $^{13}\text{CO}$  column density map and scale it with a uniform  $^{12}\text{CO}/^{13}\text{CO}$  factor of 60. In the case of the fitting formula, we derive  $^{13}\text{CO}$  column density dependent isotope ratio, and scale  $N(^{13}\text{CO})$  with the corresponding value. The assumption of a uniform isotope ratio always results in an overestimation of the “real”  $^{12}\text{CO}$  mass. If the fitting formula is applied then the overestimation could be reduced from up to  $\sim 50$  per cent to about 10 per cent.

This correlation could be used to infer isotope ratios and improve  $^{12}\text{CO}$  column density estimates based on  $^{13}\text{CO}$  observations. We note however, that the  $^{13}\text{CO}$  column density estimation methods are influenced by various sources of errors. At high column densities even the rarer isotopes become optically thick, thus provide only lower limit on the isotope column density. At low column densities, the often assumed local thermodynamic equilibrium is not suitable to calculate molecular level populations precisely, resulting in an underestimation of the column density (e.g. Padoan et al. 2000; Molina et al. 2014)

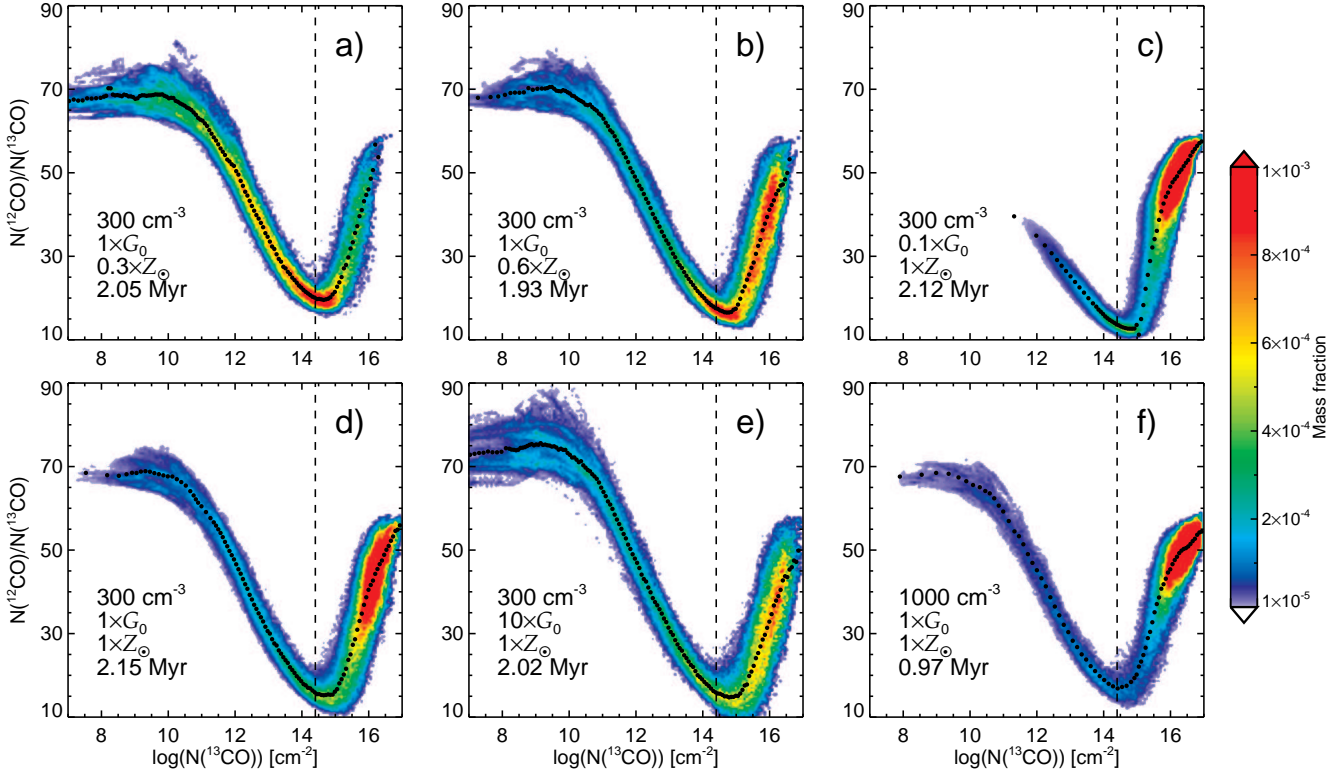


**Figure 7.** CO isotope column density ratio as a function of the  $^{13}\text{CO}$  column density. Colours and the dashed line have the same meaning as in Fig. 4. The main difference compared to Fig. 4 is the steeper slope at column densities larger than the characteristic column density of the dip in the isotope ratio.

**Table 4.** Total  $^{12}\text{CO}$  mass derived with various assumptions on the  $^{12}\text{CO}$  column density (see section 3.4). Positive per cent errors mean overestimation of the self-consistent value.

Model	$^{12}\text{CO}$ mass [ $M_{\odot}$ ]			Per cent error [%]	
	“Real”	Uniform ratio	Fitting formula	Uniform ratio	Fitting formula
a	0.433	0.702	0.447	+62.2	+3.3
b	2.529	3.937	2.961	+55.6	+17.0
c	16.016	20.345	16.990	+27.0	+6.1
d	8.102	11.400	9.499	+40.7	+17.2
e	3.024	4.913	4.047	+62.5	+33.8
f	16.866	20.132	17.782	+19.4	+5.4

#### 4 EMISSION MAPS

In the previous sections we showed that (photo-)chemical processes have a large impact on the  $^{12}\text{CO}/^{13}\text{CO}$  ratio in GMCs and that there is a clear correlation between  $N(^{12}\text{CO})$ ,  $N(^{13}\text{CO})$  and the ratio. We now explore how these effects are reflected in the observable emission maps. Could the assumption of uniform isotope ratio still give back approximately the right answer when optical depth effects and detection limits are considered? We try to answer this question quantitatively by comparing emission maps produced from self-consistent calculations with those obtained by either adopting a uniform isotope ratio, or one that depends on  $N(^{12}\text{CO})$ .

The numerical models are transformed to the observa-

tional plane by line radiative transfer modelling. We calculate the emission in a  $\pm 6 \text{ km s}^{-1}$  velocity range around the  $J = 1 \rightarrow 0$  transition of  $^{13}\text{CO}$  ( $\lambda_0 = 2720.41 \mu\text{m}$ ). For the  $^{13}\text{CO}$  number density we adopt three distributions: one produced by self-consistent simulations, a second produced by rescaling the  $^{12}\text{CO}$  distribution with a uniform isotopic ratio of 60 and a third produced by rescaling the  $^{12}\text{CO}$  distribution using the isotope ratios we obtained from our fitting formula. In the last case, we assume that the isotope ratio is constant along a given line of sight.

In the interstellar medium, the assumption that molecule energy levels are populated according to a thermal distribution (i.e. local thermodynamic equilibrium), is often invalid. To account for non-LTE conditions we used the Large Velocity Gradient (LVG) approximation, described in detail in Ossenkopf (1997) and Shetty et al. (2011a). The non-thermal excitation/de-excitation is mainly driven by collisions with other molecules or atoms. As the most abundant particle in the dense ISM, the hydrogen molecule is the most probable collisional partner for CO. We account for the two spin isomers of the hydrogen molecule using a mixture of ortho- (75 per cent) and para-hydrogen (25 per cent). The collisional rates are adopted from the Leiden Atomic and Molecular Database<sup>4</sup> (Schöier et al. 2005; Yang et al. 2010). In addition to the LVG approximation, in which the escape probability of a photon emitted by a given transition depends on the velocity gradient of the neighbouring cells,

<sup>4</sup> <http://home.strw.leidenuniv.nl/~moldata/>

**Table 5.** Total  $^{13}\text{CO}$  mass in the analysed simulation domain when its number density is self-consistently calculated or inferred from  $^{12}\text{CO}$  with a uniform isotope ratio or using our fitting formula. Negative (positive) per cent errors mean underestimation (overestimation) of the self-consistent value.

Model	$^{13}\text{CO}$ mass [ $M_{\odot}$ ]			Per cent error [%]	
	“Real”	Uniform ratio	Fitting formula	Uniform ratio	Fitting formula
a	0.012	0.008	0.014	-38.3	+12.0
b	0.068	0.044	0.068	-35.7	+0.2
c	0.351	0.277	0.369	-21.3	+5.1
d	0.197	0.140	0.190	-28.9	-3.3
e	0.085	0.052	0.073	-38.5	-13.8
f	0.348	0.291	0.345	-16.2	-0.7

we also consider the escape probability of photons due to the finite size of the cloud. For the latter, the smallest column density that a given cell “sees” must be given. Here we adopt a constant length scale of 5 pc (roughly the radius of the cloud) through the whole domain and calculate the column density based on this length and the local number density. This approach results in underestimated escape probabilities in the high density regions of the cloud.

For the radiative transport calculations we use the RADMC-3D<sup>5</sup> code (Dullemond 2012). The input parameters of the calculation are the number density of the modelled species ( $^{13}\text{CO}$  in our case), the number density of the collision partners (ortho- and para-hydrogen molecules), the gas temperature, resolved and unresolved (micro-turbulent) velocity of the gas, and the line properties (energy levels, statistical weights, Einstein A-coefficients and collision rate coefficients). The SPH data of number densities, gas velocity and temperature are interpolated to a regular grid of  $(512 \text{ pixel})^3$  as described in section A and used as the input. The micro-turbulent velocities, accounting for the unresolved velocity field, are set uniformly according to Larson’s law by  $v_{\text{mturb}} = 1.1 \times (0.032 \text{ [pc]})^{0.38} [\text{km s}^{-1}]$  (Larson 1981), where 0.032 pc is the linear size of a pixel. The line properties were adopted from Yang et al. (2010). The two dimensional intensity maps are calculated with a velocity resolution of  $0.09 \text{ km s}^{-1}$ .

We consider three different distributions for the  $^{13}\text{CO}$  number density when producing our synthetic emission maps. The first of these is taken directly from our simulation, and hence fully accounts for the effects of chemical fractionation and selective photodissociation. The second distribution is generated by scaling the  $^{12}\text{CO}$  number densities in our simulation by a uniform factor of 1/60. Finally, the third distribution is produced by scaling the  $^{12}\text{CO}$  number densities by a variable factor derived using the isotope ratio- $^{12}\text{CO}$  column density fitting function (equation 4). In the latter case, we first calculate the  $^{12}\text{CO}$  column density along the  $z$  direction, then use the fitting formula described in section 3.3 to estimate the average line-of-sight isotope ratio. In the final step, the  $^{13}\text{CO}$  number density is calculated from the  $^{12}\text{CO}$  number density and the  $^{12}\text{CO}$  column

density dependent isotope ratio. Table 5 summarizes the total  $^{13}\text{CO}$  mass for every model and each method used to calculate the  $^{13}\text{CO}$  number density distribution. These values represent the input number density distributions for the radiation transfer calculations (i.e. no radiation transfer effects are considered). It is clear from the per cent errors that the fitting formula gives a better representation of the “real”  $^{13}\text{CO}$  mass: the uniform scaling of the  $^{12}\text{CO}$  number density results in an error ranging from 15 to 40 per cent, while when using the fitting formula, the deviation is typically less than 14 per cent. When adopting a uniform isotope ratio, we always underestimate the total  $^{13}\text{CO}$  mass. The fitting formula may result in under- or overestimation with comparable absolute errors, and provides the worst match in case of the lowest metallicity or the highest radiation field strength.

#### 4.1 Comparison of emission maps

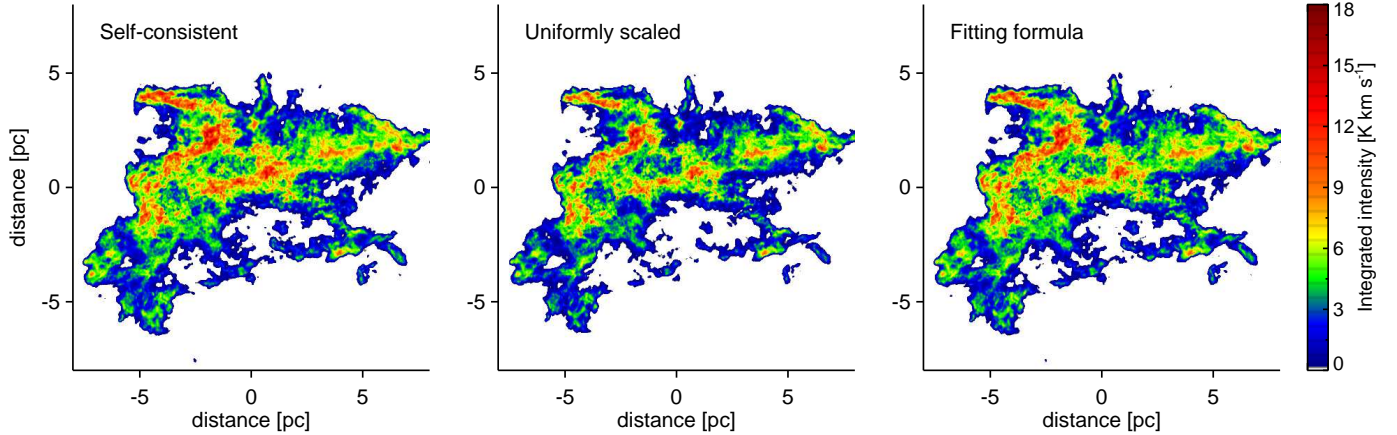
The results of the radiative transfer calculations are position-position-velocity intensity maps in units of  $\text{erg cm}^{-2}\text{s}^{-1}\text{Hz}^{-1}\text{ster}^{-1}$ . As the first step the intensity is converted to brightness temperature ( $T_b$ , in K), a quantity usually measured in molecular line observations. Then it is integrated in velocity space along the line of sight to obtain the zeroth moment maps,  $W(^{13}\text{CO})$ , in units of  $\text{K km s}^{-1}$ . For the purpose of the comparison we consider pixels with  $W(^{13}\text{CO}) > 0.2 \text{ K km s}^{-1}$  in a given map. This limit is comparable to the  $0.18 \text{ K km s}^{-1} \ 3\sigma$  level of Goldsmith et al. (2008) in the Taurus molecular cloud. This detection limit approximately translates to a  $N(^{12}\text{CO})$  of  $6 \times 10^{15} \text{ cm}^{-2}$ , suggesting a negligible effect of preferential photodissociation and a more important role of chemical fractionation in the maps above the limit. We do not consider additional noise in the synthetic maps. See Fig. 8 for the zeroth moment maps of run d), calculated with the different assumptions for the  $^{13}\text{CO}$  number density distributions.

Figure 9 compares the total intensity of pixels falling in a brightness temperature bin (with the bin size of  $0.5 \text{ K km s}^{-1}$ ) as a function of brightness temperature for the self-consistent (filled histogram with black outline) and approximate maps (orange dotted and blue dashed for the uniform ratio and fitting formula respectively). The bins with the high total intensity values contribute the most to the total emission. The contribution is determined by the enclosed area of contours associated with the lower and upper boundaries of a bin and the “mean” bin intensity. In case of simulation d), for example, the total intensity at high brightness temperatures is low because of the small area occupied by high intensity pixels. At low brightness temperatures, the corresponding area is large, but the mean intensity of pixels is low. The largest intensity contribution comes from pixels with values around  $5 \text{ K km s}^{-1}$ , due to the large area occupied and the relatively high mean intensity. The  $5 \text{ K km s}^{-1}$  brightness temperature corresponds to  $N(^{13}\text{CO}) \approx 1 \times 10^{16} \text{ cm}^{-2}$ ,  $N(^{12}\text{CO}) \approx 5 \times 10^{17} \text{ cm}^{-2}$ , and approximately  $8.6 \times 10^{21} \text{ cm}^{-2}$  total column density (in simulation d). Taking the relatively large area into account, a significant fraction of the  $^{13}\text{CO}$  and total cloud mass is associated with this intensity range.

To quantify the deviations from the self-consistent distribution, we plot the per cent errors of the approximate

<sup>5</sup> <http://www.ita.uni-heidelberg.de/~dullemond/software/radmc-3d/>





**Figure 8.** Velocity integrated  $^{13}\text{CO } J = 1 \rightarrow 0$  emission maps derived from run d) in case of the three methods. Pixels in a given map with intensity values less than the chosen detection limit of  $0.2 \text{ K km s}^{-1}$  are shown in white. The area associated with an emission value is more extended in the self-consistent map than when a uniform  $^{12}\text{CO}/^{13}\text{CO}$  isotopic ratio is assumed. The difference is most prominent at the edge of the cloud (blue region) and in the region of moderate intensity ( $4\text{--}7 \text{ K km s}^{-1}$ , green and yellow). The latter region contributes the most to the total, spatially and velocity integrated intensity of the cloud. The map produced using our fitting formula agrees well with the self-consistent case.

maps on the upper panels of figure 9. At the highest intensities the per cent error shows large fluctuation in both approximate cases. On one hand, the number of pixels in these bins are usually below- or at a few times 10. On the other hand, the  $^{12}\text{CO}/^{13}\text{CO}$  ratio falls below 60 even at the highest intensities/column densities (see Fig. 6). Hereafter we exclude bins containing fewer than 100 pixels (a solid, vertical black lines on the per cent error panels) from the comparison.

Generally, the assumption of uniform isotope ratio results in an up to  $\sim 50$  per cent underestimation at intermediate and high intensities ( $W > 2 \text{ K km s}^{-1}$ ) and slight overestimation at low intensities ( $\sim 1 \text{ K km s}^{-1}$ ). The fitting formula offers a better fit with an error usually lower than  $\sim 20$  per cent. These errors are comparable to the errors on the scaled (i.e. uniformly or  $^{12}\text{CO}$  column density dependently) input  $^{13}\text{CO}$  mass (Table 5) used in the radiation transport modelling.

The reason for the relatively large difference between the self-consistent and uniformly-scaled maps is that the area associated with a certain  $^{13}\text{CO}$  column density is systematically underestimated when the uniform isotope ratio is adopted. When isotope-selective reactions are taken into account, we find higher  $^{13}\text{CO}$  number densities at given total and  $^{12}\text{CO}$  column densities on the intermediate range. In terms of excitation conditions, this means a slight reduction in the number density of collisional partners for the  $^{13}\text{CO}$  molecules. On the other hand, the kinetic temperature is also slightly higher in these regions. This results on average in a larger volume with similar excitation conditions and emerging brightness temperature. When self-consistent and uniformly scaled maps are visually compared we find a more extended emission in the former case (see Fig. 8). When using the fitting formula, the extended emission is almost completely recovered.

The error distributions on the upper panels of Fig. 9 show environment dependent trends: in case of simulation c) and f) the per cent error is moderate in both cases (be-

low 20 per cent). In these simulations the isotope-selective photodissociation and the fractionation reaction play a relatively minor role due to the weak ISRF or the high density (the gas is well shielded close to the cloud edge) and the CO isotope ratio is close to the initial  $^{12}\text{C}/^{13}\text{C}$  ratio in regions where most of the CO mass resides (see Fig. 2). There is however a qualitative difference between runs c) and f): in the case of run c) the chemical fractionation-dominated region is extended, but due to its low column density, falls below the detection limit. In run f), on the other hand, the corresponding region is very compact. In simulation a), b), d) and e) both isotope-selective processes are important and the fitting formula recovers the self-consistent distribution better.

We conclude that above the  $0.2 \text{ K km s}^{-1}$  detection limit only chemical fractionation has a non-negligible effect on the isotope ratio, and therefore on the synthetic  $^{13}\text{CO}$  emission maps. The assumption of a uniform isotope ratio leads to an error as high as 50 per cent in  $W(^{13}\text{CO})$  at brightness temperatures above  $\sim 2 \text{ K km s}^{-1}$  in most case. This approach is a good approximation only when the ISRF is weak, or when the initial density is high. The fitting formula provides a better fit to the self-consistent map in all cases and we recommend its usage in all quantitative investigations.

## 5 COMPARISON TO PREVIOUS WORKS

The previous works of Liszt (2007) and Röllig & Ossenkopf (2013) focus on CO fractionation in diffuse clouds and photon dominated regions (PDR), respectively. The former study concludes that the CO isotope ratio is determined by the competing processes of selective photodissociation and chemical fractionation and that the ratio does not reflect local properties, such as the CO excitation temperature and gas density. Röllig & Ossenkopf (2013) find a different behaviour in PDR models: with the exception of very

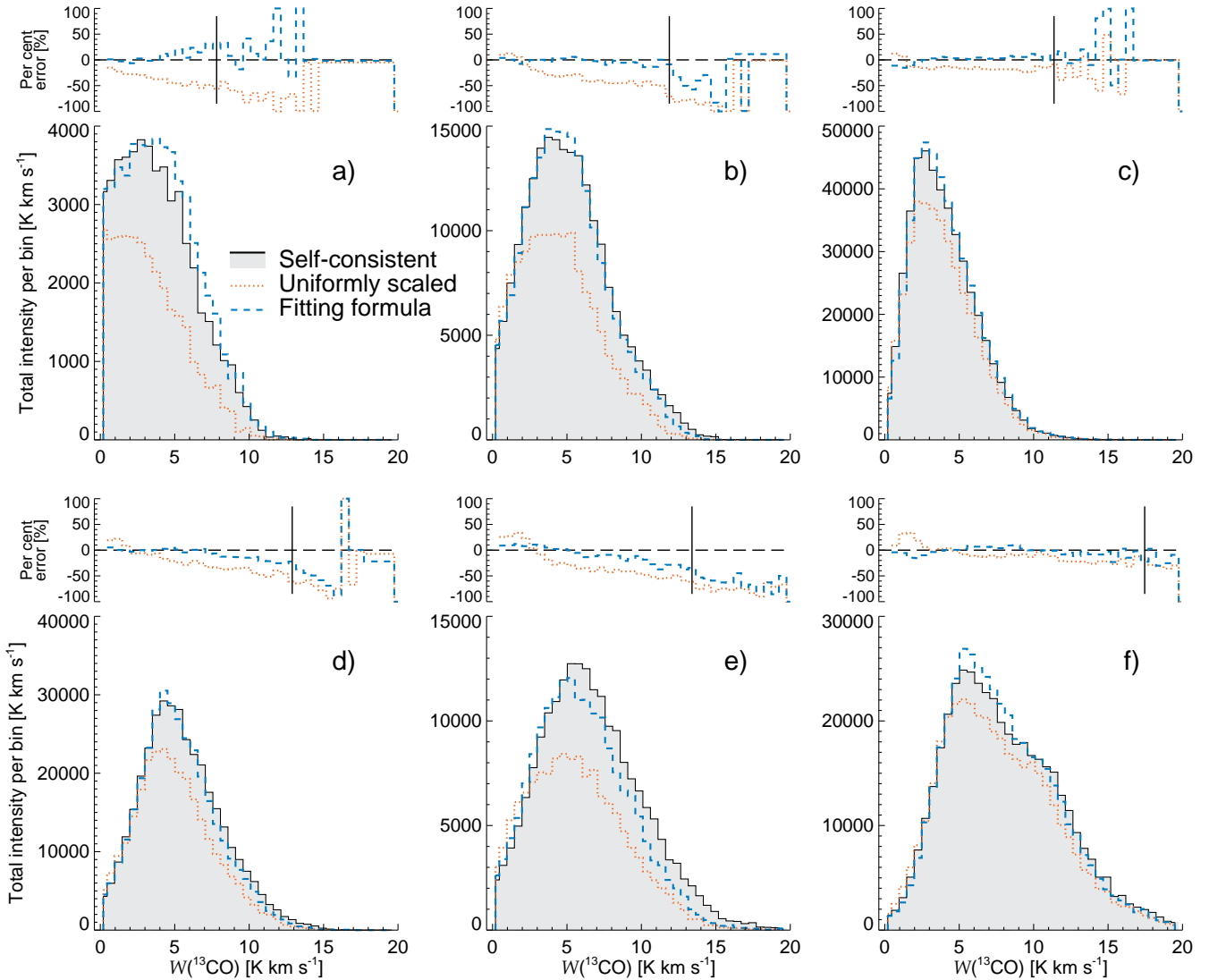


**Figure 9.** Comparison of the  $^{13}\text{CO}$  ( $J = 1 \rightarrow 0$ ) brightness temperature distributions in our 6 simulations. The figure shows which brightness temperatures are contributing the most to the total intensity of the cloud. The filled histograms with the black outlines show the self-consistent models. The orange dotted and blue dashed lines represent the distributions from the uniformly scaled and fitting formula approximations. The per cent errors of the later compared to the self-consistent distribution are shown on panels above the intensity distributions. The vertical black line marks the intensity below which each bin contains more than 100 pixels. We only considered pixels with  $W(^{13}\text{CO}) > 0.2 \text{ K km s}^{-1}$ .

specific parameters, the  $^{12}\text{CO}/^{13}\text{CO}$  ratio is always smaller than the  $^{12}\text{C}/^{13}\text{C}$  elemental ratio, indicating that isotope-selective photodissociation is much less effective than chemical fractionation over the whole PDR. The common feature of these studies is that they use simplified geometry and density distributions and scale the radiation field strength and the density to probe a large parameter range.

We present cloud simulations with self-consistently calculated density, velocity and temperature structure, which is expected to be consistent with isolated molecular clouds before star formation kicks in. The CO isotope ratio in our simulations shows a behaviour more consistent with the results of Liszt (2007). The upper and lower panels of Fig. 10 show the fractional abundances of carbon bearing species and their isotopic abundance ratios as the function of visual extinction respectively. The figure could be directly com-

pared to Fig. 3 and 4 in Röllig & Ossenkopf (2013) (note that here we show a cloud with an ISRF 10 times lower than in their figures). At low and high visual extinctions most of the carbon atoms are locked in  $\text{C}^+$  and CO, respectively. The transition  $A_V$  is at  $\sim 1.5$  mag. Increasing radiation field strength or decreasing the metallicity shifts this towards higher values. Compared with the PDR models, the most prominent difference is that the  $\text{C}^+$ -CO transition is located at about an order of magnitude larger  $A_V$ . In contrast with those models, we also find CO isotope ratios above the elemental ratio at low  $A_V$ . This is a consequence of significant isotope-selective photodissociation in low column density (or  $A_V$ ) regions, where the gas temperature is above 40 K (see lower panel of Fig. 10). The differences between our results and those of Röllig & Ossenkopf (2013) appear to be an outcome of the different physical conditions adopted

in the two studies. Röllig & Ossenkopf (2013) considers gas densities significantly higher than our mean cloud densities, and hence finds much lower temperatures in the low  $A_V$  gas than we do here. This significantly enhances the effectiveness of chemical fractionation in their models, resulting in lower isotope ratios at low  $N(^{12}\text{CO})$ .

On the observational side, Burgh et al. (2007), Sheffer et al. (2007) and Sonnentrucker et al. (2007) provide ultraviolet absorption measurements of the  $\text{H}_2$ ,  $^{12}\text{CO}$ ,  $^{13}\text{CO}$  column densities and consequently the  $^{12}\text{CO}/^{13}\text{CO}$  isotopic ratio. Liszt & Lucas (1998) also determined the CO isotope ratio in nine selected line of sights by measuring millimetre-wavelength absorption and emission. Both the UV absorption and millimetre-wavelength measurements are limited to  $^{12}\text{CO}$  column densities in the range  $10^{14} \text{ cm}^{-2} < N(^{12}\text{CO}) < 4 \times 10^{16} \text{ cm}^{-2}$ . At higher column densities the  $^{12}\text{CO}$  absorption/emission saturates, preventing the direct measurement of its column density. At these CO column densities, Goldsmith et al. (2008) fitted the brightness temperature distribution of  $^{12}\text{CO}$  and  $^{13}\text{CO}$  emission from the Taurus molecular cloud, using a grid of PDR models with the assumption of an increasing  $^{12}\text{CO}/^{13}\text{CO}$  abundance ratio with increasing  $N(^{12}\text{CO})$ . Although this method carries significant uncertainties, their results provide valuable constraints on the isotope ratio at high CO column densities.

The aforementioned observations are summarized and compared with our fitting formula and run d) in Fig. 11. The UV measurements are inconsistent with the proposed fitting formula, while the millimetre-wavelength measurements and the fitted ratios are largely consistent with it. When interpreting UV absorption data one should keep in mind that, in contrast with millimetre-wavelength data, contributions of individual clouds in the considered line of sight cannot be identified, and thus such measurements are not tracing properties of individual clouds. This overlap effect might be responsible for the tendency towards higher ratios from UV measurements, as the individual clouds contributing to the measured  $N(^{12}\text{CO})$  will have smaller column densities and higher isotope ratios.

An other possible explanation might be that the UV absorption measurements are tracing molecular clouds which are more similar to the models of photon dominated regions. Röllig & Ossenkopf (2013) for example, finds CO isotope ratios measured by ultraviolet absorption to be qualitatively consistent with their models on the sampled parameter range.

## 6 SUMMARY

We investigate the effects of selective photodissociation and chemical fractionation on the  $^{12}\text{CO}/^{13}\text{CO}$  ratio in realistic hydrodynamical simulations of isolated molecular clouds, considering a range of cloud properties. We aim to quantitatively test the validity of the frequently assumed uniform isotope ratio, when  $^{13}\text{CO}$  intensities are calculated from hydrodynamical simulations neglecting isotopic chemistry or when  $^{12}\text{CO}$  column density/mass is inferred from observations of  $^{13}\text{CO}$  emission.

We find a close correlation between the  $^{12}\text{CO}$  column density and the isotope ratio, which shows only a weak dependence on cloud conditions within the considered param-

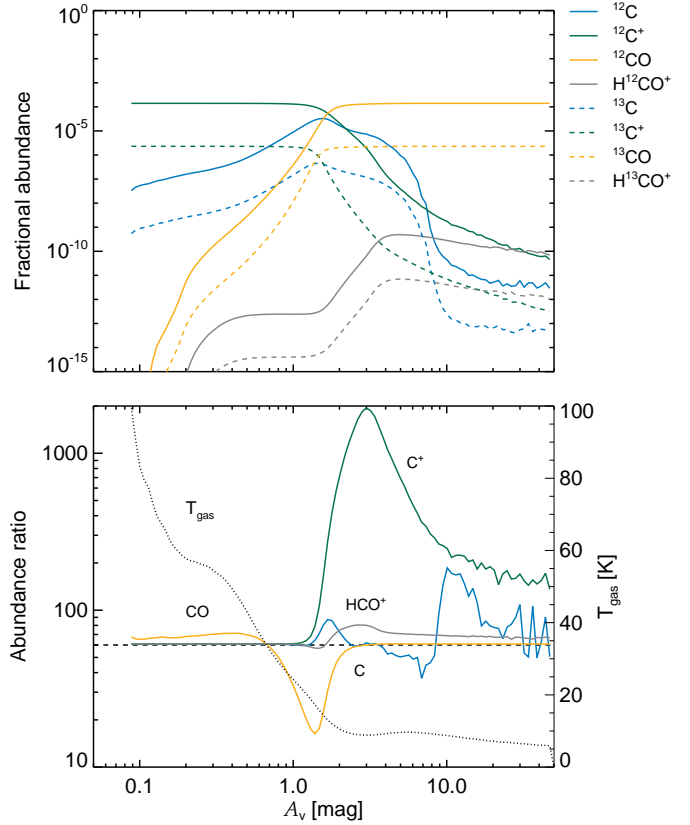


**Figure 10.** The upper panel shows the fractional abundances (relative to total hydrogen nuclei) of the main carbon bearing species and their isotopes as functions of the mean visual extinction in the case of run d). The lower panel shows the median isotopic abundance ratios as a function of visual extinction. The dashed line shows the elemental carbon isotope ratio. The dotted line is the median gas temperature at a given visual extinction. The large fluctuations in the isotope ratio of neutral atomic carbon at high visual extinctions are not physical and result from  $^{13}\text{C}$  abundances that are as low as the numerical precision of the chemical kinetics solver.

eter range. At  $^{12}\text{CO}$  column densities below  $\sim 10^{12} \text{ cm}^{-2}$  selective photodissociation increases the isotope ratio up to 70. Millimetre-wavelength CO emission from these regions is usually below the currently achievable detection limits ( $\sim 0.2 \text{ K km s}^{-2}$ ), and therefore the selective photodissociation has limited impact on observable properties. The chemical fractionation reaction – by enhancing the  $^{13}\text{CO}$  abundance – reduces the isotope ratio to values as small as 20 in the  $10^{15} \text{ cm}^{-2} < N(^{12}\text{CO}) < 10^{17} \text{ cm}^{-2}$  range. At high CO column densities neither of the isotope-selective reactions are effective, therefore the ratio increases to the value of the elemental isotopic abundance ratio. The isotope ratio varies similarly with the  $^{13}\text{CO}$  column density.

The correlations show a weak dependence on environmental conditions because with stronger irradiation or lower metallicity the regions of significant  $^{12}\text{CO}$  and  $^{13}\text{CO}$  formation shift towards higher total column densities by a similar amount. Besides this, the characteristic gas temperatures of regions where CO reside are very similar in every simulation.

If  $^{12}\text{CO}$  number densities are provided (e.g. from a sim-



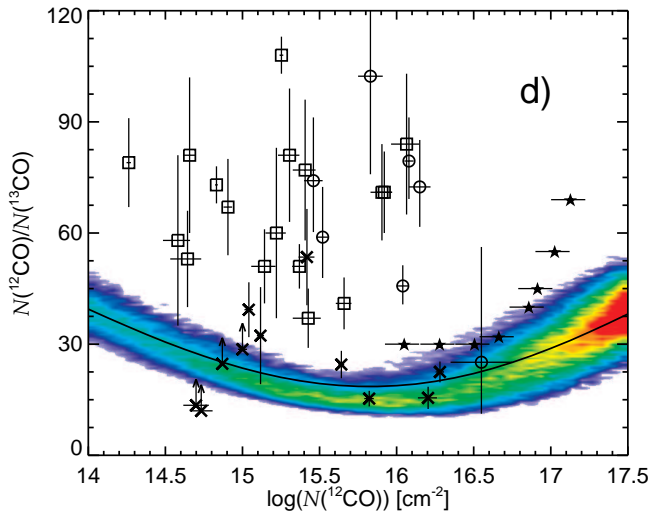


**Figure 11.**  $^{12}\text{CO}/^{13}\text{CO}$  column density ratios from the literature compared to run d) and the adopted fitting formula (black solid line). The ultraviolet absorption measurements are from Sheffer et al. (2007, open square) and Sonnentrucker et al. (2007, open circle). The millimetre-wavelength data are from Liszt & Lucas (1998, “x” symbol). The filled stars are *not direct measurements* but values derived by absorption line profile fitting presented in Goldsmith et al. (2008). The colour scale is the same as in Fig. 4. In contrast to the UV absorption measurements, the millimetre-wavelength data and the fitted ratios are largely consistent with the fitting formula and the distribution in the simulation.

ulation of a molecular cloud, such as in Glover & Clark (2012a), and if we want to calculate the corresponding  $^{13}\text{CO}$  number densities, then using a uniform  $^{12}\text{CO}/^{13}\text{CO}$  ratio results in the  $^{13}\text{CO}$  number densities being underestimated by as much as 40–50 per cent (see Table 5). This can lead to errors of up to 50 per cent in some regions of the derived  $^{13}\text{CO}$  integrated intensity maps (see Fig. 9). In section 3.3 we derive a fitting formula based on the simulation results to address this issue in a computational cost efficient way (i.e. to infer the correct ratio without the need of the full fractionation chemistry model). When the fitting formula is applied, then the  $^{13}\text{CO}$  column/number density and emission can be recovered with errors smaller than 15–20 per cent.

If we have instead  $^{13}\text{CO}$  column densities (e.g. derived from observations), then using a uniform  $^{12}\text{CO}/^{13}\text{CO}$  ratio to convert them to  $^{12}\text{CO}$  column densities may result in the overestimation of the  $^{12}\text{CO}$  column densities, again by up to 50–60 per cent (see Table 4). In section 3.4 we construct a fitting formula describing the correlation of the isotope ratio and the  $^{13}\text{CO}$  column density. By applying this formula the errors could be reduced to  $\sim 10$  per cent. We note however, that the error introduced by using a fixed  $^{12}\text{CO}/^{13}\text{CO}$  ratio may be smaller than other sources of errors in the determination of the  $^{13}\text{CO}$  column density (such as the assumption that the excitation temperatures of  $^{12}\text{CO}$  and  $^{13}\text{CO}$  are the same and that the  $^{13}\text{CO}$  emission is optically thin), which can lead to uncertainties of as much as a factor of 4 (see Padoan et al. 2000). Nevertheless, in the  $10^{14} \text{ cm}^{-2} < N(^{13}\text{CO}) < 10^{16} \text{ cm}^{-2}$  range, where the aforementioned assumptions are valid and the chemical fraction-

ation is effective, the fitting formula provides more accurate conversion to  $^{12}\text{CO}$  than the assumption of uniform scaling.

The proposed fitting formulas are consistent with millimetre-wavelength  $^{12}\text{CO}/^{13}\text{CO}$  column density ratio measurements, and underestimate the ratio measured in ultraviolet absorption by a factor of 2–3 (see Fig. 11). The reason for the discrepancy with the ultraviolet data might be that the UV measurements are not tracing individual clouds, but an accumulation of low density material along the line of sight or that physical properties of the traced clouds are fundamentally different from those discussed here (e.g. more similar to PDR regions).

Finally, we conclude that the fitting formulas proposed above are good representations of the  $^{12}\text{CO}/^{13}\text{CO}$  isotopic ratio distributions of our hydro-chemical simulations and that they can be used to infer  $^{13}\text{CO}$  properties from (magneto-)hydrodynamical simulations in a computationally cost-efficient manner, and more precise  $^{12}\text{CO}$  column density estimates from  $^{13}\text{CO}$  observations, provided that the molecular clouds under investigation are similar to those presented here.

## ACKNOWLEDGEMENTS

The authors acknowledge support from the Deutsche Forschungsgemeinschaft via SFB project 881 “The Milky Way System” (sub-projects B2 and B3). The numerical simulations were partly performed on the KOLOB cluster at the University of Heidelberg and partly on the Milky Way supercomputer, funded by the DFG through Collaborative Research Center (SFB 881) “The Milky Way System” (sub-project Z2), hosted and co-funded by the Jülich Supercomputing Center (JSC). R.S.K. acknowledges support from the European Research Council under the European Community’s Seventh Framework Programme (FP7/2007–2013) via the ERC Advanced Grant STARLIGHT (project number 339177).

## REFERENCES

- Audouze, J., Lequeux, J., & Vigroux, L., 1975, *A&A*, 43, 71
- Bate, M. R., Bonnell, I. A., & Price, N. M., 1995, *MNRAS*, 277, 362
- Beaumont, C. N., Offner, S., Shetty, R., Goodman, A., Glover, S. C. O., 2013, *ApJ*, 777, 173
- Black, J. H., 1994, *ASP Conf. Ser.* 58, in *The First Symposium on the Infrared Cirrus and Diffuse Interstellar Clouds*, eds. R. M. Cutri & W. B. Latter, (San Francisco:ASP), 355
- Bohlin, R. C., Savage, B. D., Drake, J. F., 1978, *ApJ*, 224, 132
- Clark, P. C., Glover, S. C. O., Klessen, R. S., 2012, *MNRAS*, 420, 745
- Burgh, E. B., France, K., McCandliss, S. R., 2007, *ApJ*, 658, 446
- Dullemond, C. P. 2012, *Astrophysics Source Code Library*, 2015
- Draine, B. T., 1978, *ApJS*, 36, 595
- Draine, B. T., & Bertoldi, F., 1996, *ApJ*, 468, 269

Draine, B. T., 2003, *ApJ*, 598, 1026  
 van Dishoeck, E. F., Black, J. H., 1988, *ApJ*, 334, 771  
 Federrath, C., Banerjee, R., Clark, P. C., Klessen, R. S., 2010 *ApJ*, 713, 269  
 Feldmann, R., Gnedin, N. Y., Kravtsov, A. V., 2012, *ApJ*, 747, 124  
 Geiss, J., 1988, *Reviews in Modern Astronomy* 1, ed. G. Klare (Heidelberg: Springer-Verlag), pp. 1-27  
 Goto, M., Usuda, T., Takato, N., Hayashi, M., Sakamoto, S., Gaessler, W., Hayano, Y., et al., 2003, *ApJ*, 598, 1038  
 Glover, S. C. O., & Mac Low, M.-M. 2007, *ApJ*, 659, 1317  
 Glover, S. C. O., Federrath, C., Mac Low, M.-M., & Klessen, R. S., 2010, *MNRAS*, 404, 2  
 Glover, S. C. O., Mac Low, M.-M., 2011, *MNRAS*, 412, 337  
 Glover, S. C. O., Clark, P. C., 2012a, *MNRAS*, 421, 9  
 Glover, S. C. O., Clark, P. C., 2012b, *MNRAS*, 421, 116  
 Goldsmith, P. F., Heyer, M., Narayanan, G., Snell, R., Li, D., Brunt, C., 2008, *ApJ*, 680, 428  
 Górski K. M., Hivon E., Banday A. J., Wandelt B. D., Hansen F. K., Reinecke M., Bartelmann M., 2005, *ApJ*, 622, 759  
 Habing, H. J., 1968, *Bull. Astron. Inst. Netherlands*, 19, 421  
 Jappsen, A.-K., Klessen, R. S., Larson, R. B., Li, Y., Mac Low, M.-M., 2005, *A&A*, 435, 611  
 Langer, W. D., 1976, *ApJ*, 212, 39  
 Langer, W. D., Penzias, A. A., 1990, *ApJ*, 357, 477  
 Larson, R. B., 1981, *MNRAS*, 194, 809  
 Lee, H.-H., Herbst, E., Pineau des Forets, G., Roueff, E., & Le Bourlot, J. 1996, *A&A*, 311, 690  
 Leroy, A. K., Bolatto, A., Gordon, K., Sandstrom, K., et al., 2011, *ApJ*, 737, 12  
 Liszt, H. S., Lucas, R., 1998, *A&A*, 339, 561  
 Liszt, H. S., 2007, *A&A*, 476, 291  
 Lucas, R., Liszt, H. S., 1998, *A&A*, 337, 246  
 Mitchell, G. F., & Maillard, J.-P., 1993, *ApJ*, 404, L79  
 Molina, F., Glover, S. C. O., Shetty, R., Klessen, R. S., 2014, *MNRAS*, in prep.  
 Nelson R. P., Langer, W. D., 1999, *ApJ*, 524, 923  
 Ossenkopf, V., 1997, *New Astronomy*, 2, 65  
 Padoan, P., Juvela, M., Bally, J., & Nordlund, Å., 2000, *ApJ*, 529, 259  
 Pineda, J. E., Caselli, P., Goodman, A. A., 2008, *ApJ*, 679, 481  
 Pineda, J. L., Goldsmith, P. F., Chapman, N., Snell, R. L., Li, D., Cambrésy, L., Brunt, C., 2010, *ApJ*, 721, 686  
 Röllig, M., Ossenkopf, V., 2013, *A&A*, 550, 56  
 Schöier, F.L., van der Tak, F.F.S., van Dishoeck, E.F., Black, J.H., 2005, *A&A*, 432, 369-379  
 Scoville, N., Klienmann, S. G., Hall, D. N. B., & Ridgway, S. T., 1983, *ApJ*, 275, 201  
 Sembach, K. R., Howk, J. C., Ryans, R. S. I., & Keenan, F. P., 2000, *ApJ*, 528, 310  
 Sheffer, Y., Rogers, M., Federman, S. R., Lambert, D. L., Gredel, R., 2007, *ApJ*, 667, 1002  
 Shetty, R., Glover, S. C., Dullemond, C. P., Klessen, R. S., 2011a, *MNRAS*, 412, 1686  
 Shetty, R., Glover, S. C., Dullemond, C. P., Ostriker, E. C., Harris, A. I., Klessen, R. S., 2011b, *MNRAS*, 415, 3253  
 Smith, D., Adams, N. G., 1980, *ApJ*, 242, 424  
 Sonnentrucker, P., Welty, D. E., Thorburn, J. A., York, D. G., 2007, *ApJS*, 168, 58

Springel, V., 2005, *MNRAS*, 364, 1105  
 Visser, R., van Dishoeck, E. F., Black, J. H., 2009, *A&A*, 503, 323  
 Wannier, P. G., Penzias, A. A., Linke, R. A., Wilson, R. W., 1975, *ApJ*, 204, 26  
 Watson, W. D., Anicich, V. G., Huntress, W. T., 1976, *ApJ*, 205, 165  
 Williams, T., Kelley, C., et al., 2011, *Gnuplot 4.5: an interactive plotting program*  
 Wilson, T. L., 1999, *Rep. Prog. Phys.*, 62, 143  
 Wilson, T. L., Rohlfs, K., Httemeister, S., 2009, in *Tools of Radio Astronomy*, Springer  
 Yang, B., Stancil, P.C., Balakrishnan, N., Forrey, R. C., 2010, *ApJ*, 718, 1062

## APPENDIX A: INTERPOLATION TO A REGULAR GRID

To interpret the results from our Lagrangian hydrodynamic simulations we interpolate the SPH particles to a regular grid. We construct a  $512^3$  grid centred on the geometrical midpoint of the uniform density sphere defined in the initial conditions. The sides of the grid are 16.2 pc long. The 2D-projected resolution of the grid is therefore  $0.032 \times 0.032$  pc<sup>2</sup>. This resolution is comparable to the current observationally achievable resolution for nearby star-forming regions in millimetre-wavelength CO line emission (e.g. 0.03 pc linear resolution for Taurus in [Pineda et al. 2010](#)). The interpolated quantities are the total volume density, the gas and dust temperatures, the velocity field and the H<sub>2</sub>, <sup>12</sup>CO and <sup>13</sup>CO number densities.

The density of a voxel (3D pixel) is accumulated from the contribution of SPH particles lying strictly within the voxel and from the contribution of those which have common section with it (i.e. particles with centre coordinates outside of the voxel could contribute). If  $r$  is the distance between the centres of the voxel and an SPH particle, the contribution is given by the following smoothing kernel:

$$W(r, h) = \frac{8}{\pi h^3} \times \begin{cases} 1 - 6(\frac{r}{h})^2 + 6(\frac{r}{h})^3 & \text{if } 0 \leq \frac{r}{h} \leq 0.5 \\ 2 \times (1 - \frac{r}{h})^3 & \text{if } 0.5 < \frac{r}{h} \leq 1 \\ 0 & \text{if } \frac{r}{h} > 1 \end{cases} \quad (\text{A1})$$

where  $h$  is the smoothing length of the particle defined according equations (5) and (6) in [Springel \(2005\)](#). The smoothing kernel has units of cm<sup>-3</sup>, and when multiplied with the particle mass gives the contribution of an SPH particle to the voxel density. In case of the other quantities the contribution is the SPH particle value multiplied by the ratio of the density contribution and the total density of the SPH particle.

The interpolation to a regular grid is necessary for the grid based radiation transfer modelling described in section 4. For consistency we also analyse the grid interpolated quantities in section 3.